Article

Cell Reports

Neutrophils and Snail Orchestrate the Establishment of a Pro-tumor Microenvironment in Lung Cancer

Graphical Abstract

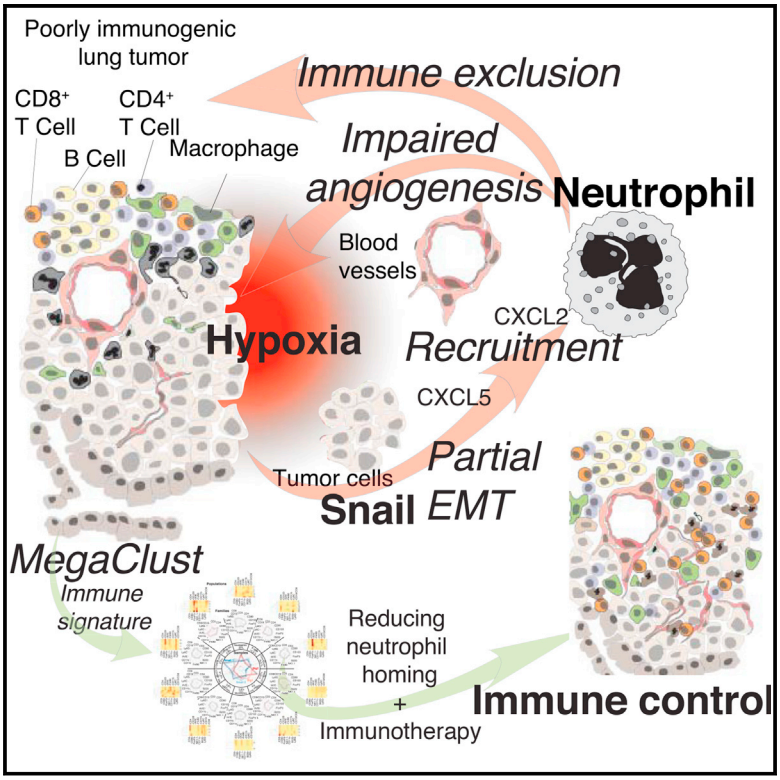

Highlights

- An unsupervised immune signature allows stratification of poorly immunogenic tumors
- Neutrophil depletion reverts immune exclusion allowing anti-PD1 treatment efficacy
- Neutrophils alter angiogenesis, increasing hypoxia and stabilizing Snail
- Snail favors neutrophil homing, induces partial EMT, and enhances tumor progression

Authors

Julien Faget, Svenja Groeneveld, Gael Boivin, ..., Alessandra Piersigilli, Ioannis Xenarios, Etienne Meylan

Correspondence

etienne.meylan@epfl.ch

In Brief

Faget et al. extract an immune signature from lung tumors pointing to neutrophils as contributors to disease progression. They show that neutrophils inhibit immunotherapy efficacy and alter angiogenesis, increasing tumor hypoxia and Snail expression. Snail enhances tumor growth and neutrophil recruitment, establishing an amplification loop favoring cancer aggressiveness.

Faget et al., 2017, Cell Reports *21*, 3190–3204
December 12, 2017
https://doi.org/10.1016/j.celrep.2017.11.052

CellPress

OPEN ACCESS
CellPress

Cell Reports
Article

Neutrophils and Snail Orchestrate the Establishment of a Pro-tumor Microenvironment in Lung Cancer

Julien Faget,[1,9] Svenja Groeneveld,[1,9] Gael Boivin,[2] Martial Sankar,[3] Nadine Zangger,[1,4] Miguel Garcia,[5] Nicolas Guex,[3] Inti Zlobec,[6] Loïc Steiner,[1] Alessandra Piersigilli,[7,8] Ioannis Xenarios,[3] and Etienne Meylan[1,10,*]

[1]Swiss Institute for Experimental Cancer Research, School of Life Sciences, Ecole Polytechnique Fédérale de Lausanne, 1015 Lausanne, Switzerland
[2]Radiobiology Laboratory, Department of Oncology, Centre Hospitalier Universitaire Vaudois, University of Lausanne, 1011 Lausanne, Switzerland
[3]Vital-IT, SIB Swiss Institute of Bioinformatics, 1015 Lausanne, Switzerland
[4]Bioinformatics Core Facility, SIB Swiss Institute of Bioinformatics, 1015 Lausanne, Switzerland
[5]Flow Cytometry Core Facility, School of Life Sciences, Ecole Polytechnique Fédérale de Lausanne, 1015 Lausanne, Switzerland
[6]Institute of Pathology, University of Bern, 3008 Bern, Switzerland
[7]Institute of Animal Pathology, University of Bern, 3012 Bern, Switzerland
[8]School of Life Sciences, Ecole Polytechnique Fédérale de Lausanne, 1015 Lausanne, Switzerland
[9]These authors contributed equally
[10]Lead Contact
*Correspondence: etienne.meylan@epfl.ch
https://doi.org/10.1016/j.celrep.2017.11.052

SUMMARY

Understanding the immune compartment of tumors facilitates the development of revolutionary new therapies. We used a *Kras(G12D)*-driven mouse model of lung cancer to establish an immune signature and identified a contribution of Gr1$^+$ neutrophils to disease progression. Depletion experiments showed that Gr1$^+$ cells (1) favor tumor growth, (2) reduce T cell homing and prevent successful anti-PD1 immunotherapy, and (3) alter angiogenesis, leading to hypoxia and sustained Snail expression in lung cancer cells. In turn, Snail accelerated disease progression and increased intratumoral Cxcl2 secretion and neutrophil infiltration. Cxcl2 was produced mainly by neutrophils themselves in response to a factor secreted by Snail-expressing tumor cells. We therefore propose a vicious cycle encompassing neutrophils and Snail to maintain a deleterious tumor microenvironment.

INTRODUCTION

Over the past 20 years, tumor infiltration by multiple immune cell populations has been shown to predict patient outcomes for many solid tumor types, and the concept of cancer immunotherapy enables new treatment strategies. Lung cancer is the leading cause of cancer-associated deaths (Ferlay et al., 2015), and first-line immunotherapy-based clinical trials yielded promising results in lung cancer patients with extensive (>50%) expression of programmed death-ligand 1 (PDL1) in the tumor cells (22%–28% of patients) (Reck et al., 2016). This heterogeneous response rate, however, suggests that the anti-tumor response cannot be harnessed in all non-small-cell lung cancer (NSCLC) cases. Formation of tertiary lymphoid structures (TLSs) concomitantly with lung cancer development indicates the presence of an active immune response (Goc et al., 2013). Previously, powerful predictions of patients' outcomes have been obtained by interrogating the impact of multiple immune cell populations together, exemplified in colon cancer (Galon et al., 2006).

Along the same line, mapping the immune compartment of lung tumors could allow better understanding of the immunologic circuits active in this malignancy. Indeed, considering the interplay between the different components of the tumor microenvironment and the carcinoma cells is essential to deciphering mechanisms driving cancer progression. For example, blood vessels and endothelial cells not only provide oxygen and nutrients but also govern immune cell extravasation into the tumor mass. Although the expression of Fas ligand (FasL) by endothelial cells impairs immune cell extravasation (Zhang et al., 2005; Motz et al., 2014), a high endothelial venule (HEV)-like phenotype facilitates immune cell adhesion and infiltration into inflamed sites, including tumors (Martinet et al., 2012).

Numerous soluble factors produced by cancer cells can also directly influence the intratumor immune compartment. For example, cancer cells undergoing epithelial-mesenchymal transition (EMT), a developmental process contributing to metastasis formation in many solid tumor types, display an immunosuppressive phenotype, as they secrete cytokines, notably TGF-β, which support the differentiation of regulatory T cells (Tregs) (Kudo-Saito et al., 2009).

In line with this, the key EMT transcription factor Snail can exert a protumorigenic influence on several immune cell populations, directly activating the expression of cytokines contributing to the recruitment of tumor-promoting M2 macrophages via CCL2 and CCL5 (Hsu et al., 2014), while impairing the function of dendritic cells and inducing Treg differentiation (Kudo-Saito et al., 2009).

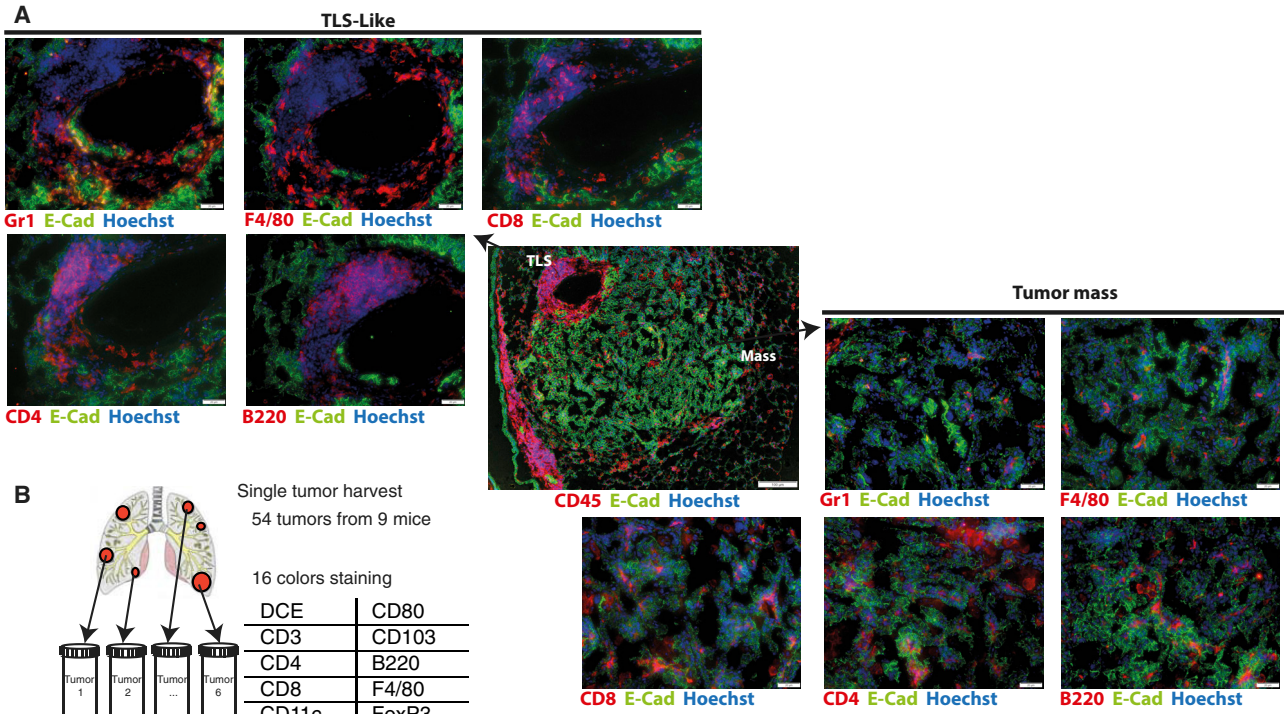

(legend on next page)

Studying this complex interplay among carcinoma cells, stromal cells, and the immune compartment requires fully immunocompetent animals. In our work, we used the inducible model of mutant *Kras*$^{LSL\text{-}G12D/WT}$; *p53*$^{FL/FL}$-driven lung adenocarcinoma (KP) (Jackson et al., 2005), in which tumors are considered poorly immunogenic because they are refractory to immune checkpoint blockade (anti-PD1 and anti-CTLA4) immunotherapy (Pfirschke et al., 2016).

RESULTS

A Dynamic Immune Response Occurs in KP Tumors

In KP mice, adaptive immunity partially controls disease progression, as KP-Rag^{ko} tumors, obtained by crossing KP mice in a *Rag1*-deficient background, displayed accelerated growth compared with normal KP tumors (Figure S1A). To elucidate the immune microenvironment in KP tumors, we monitored immune cell localization using immunofluorescence (IF). Most of the immune cells resided outside the tumor mass, forming aggregates of CD45$^+$ cells, and were in close proximity with tumors, blood vessels, and airways. Those lymphoid structures were composed mostly of B cells (B220$^+$) and CD4$^+$ and CD8$^+$ T lymphocytes surrounded by macrophages (F4/80$^+$) and Gr1 (Ly6G-C) positive cells. To a lower extent, we also found all of these immune populations isolated or as small clusters infiltrating the tumor mass (Figure 1A).

We then aimed to establish an immune signature from the KP tumors by flow cytometry. To this end, we developed a 16-color flow cytometry staining allowing the identification of 60 immune cell populations and monitored the immune infiltration in 54 resected tumors ranging from very small (9 mg) to very large (330 mg) (Figure 1B). We manually analyzed the flow cytometry data using an exclusion-based rational gating strategy in which each event can be annotated only once and almost 100% of the immune cells are assigned to one of the subpopulations (Figures 1C, S1B, and S1C).

The resulting average immune compartment (CD45$^+$ cells) was characterized by a predominance of myeloid cells (51% ± 10%), composed mostly of CD11b$^+$Ly6G$^+$Ly6C$^+$ neutrophils (17.9% ± 10.2%), F4/80$^+$ macrophages (15.4% ± 9.6%), and CD11c$^+$ dendritic cells (DCs; 15.3% ± 9.6%). Four DC subpopulations could be distinguished regarding CD11b and CD103 expression. Most of the major histocompatibility complex class II (MHC-II) (IA/IE)$^+$CD80$^+$-activated antigen-presenting cells (8.9% ± 6.3% of the immune compartment) were found among CD11b$^+$ DCs and macrophages. Ly6C$^+$CD11c^{int}CD11b$^+$ cells and CD11b$^+$Ly6C^{hi} monocytes were rare (1.8% ± 0.9% and 2.3% ± 1.6%, respectively). Lymphoid cells represented 37% ± 12% of the immune compartment and were composed mostly of CD3$^+$ T lymphocytes (19.4% ± 11.7%) and B220$^+$ CD19$^+$ B lymphocytes (11.6% ± 7.8%). In these tumors, NK1.1$^+$ natural killer (NK) cells and NK-T cells were rare (2% ± 1.5% and 0.1% ± 0.08%, respectively). Among the CD4$^+$ T cells (11.4% ± 6.1%), the FoxP3$^+$ Tregs (7.9% of CD4$^+$ T cells) contained a strong proportion of CD103$^+$IA/IE$^+$ cells, and the proportion of CD8$^+$ T cells was low (3.3% ± 3.4%) (Figure 1D; Table S1). The immune signature from tumors compared with healthy lung differed substantially (Figure S1D). Additionally, we observed a strong inverse correlation between the proportion of immune cells (CD45$^+$) and tumor size (Figure S1E).

The Immune Signature Predicts Tumor Size and Identifies Neutrophils as Potential Contributors of Disease Progression

Histopathological analyses of KP lung sections revealed heterogeneity of lesions, as benign and advanced lesions were found within the same animal, with the most advanced histological grades (adenocarcinoma grades 4 and 5) predominantly found in the largest tumors (Figures S2A and S2B). We therefore hypothesized that we can identify changes in the immune signature that are associated with tumor progression and inter-lesion heterogeneity.

To validate the accuracy of the method, we first analyzed tumors with a putatively different immune compartment. To do so, we generated a model of immunogenic KP tumors (designated KP-Im), in which the lentiviral vector used for tumor initiation codes for GFP-ovalbumin (OVA) in addition to Cre, mimicking tumor cell-specific expression of strong tumor antigens. Consistently with previous immunogenic KP models (DuPage et al., 2011), micro-computed tomographic (μCT) imaging revealed a delayed growth of KP-Im compared with KP tumors (Figure S2C). We also analyzed KP tumors of mice treated with pemetrexed (KP-Pem), a conventional chemotherapy, to model a chemically driven systemic impact on the host. The comparison with KP tumors revealed detectable changes in the composition of infiltrating immune cells in KP-Im and KP-Pem tumors (Figure S2D; Tables S1 and S2). Unsupervised clustering of the samples on the basis of their immune signature correctly assigned them to their respective group in most cases (Figure S2E).

Among normal KP tumors, unsupervised sample clustering on the basis of the abundance of 48 immune cell populations generated three groups (small [S], Mix1, and Mix2), stratifying tumors according to their weight (Figure 2A). Because multistep gating such as the manual exclusion-based gating strategy described above relies on the selection of specific markers to define immune populations, and the gating itself can be criticized for its subjectivity, we developed an automated algorithm, MegaClust (http://megaclust.vital-it.ch), which identifies cell populations from complex cytometry datasets (see Supplemental Experimental Procedures). An evaluation of the quality of each cell population identified by MegaClust was included in the workflow and performed considering (1) its proximity to the filtration gates (manual selection of viable CD45$^+$ immune cells), (2)

Figure 1. KP Tumors Have a Complex Immune Environment

(A) IF staining on serial lung sections from tumor-bearing KP mice 18 weeks post-tumor initiation. Panels show multiple immune populations forming a TLS-like structure surrounding a blood vessel (top left) or within the tumor mass (bottom right). The scale bars represent 50 μm (central picture, 100 μm).

(B) Experimental design and flow cytometry. DCE, dead cell exclusion.

(C) Gating strategy used to analyze flow cytometry data.

(D) Results from three levels of gating represent the average percentage of the indicated cell populations.

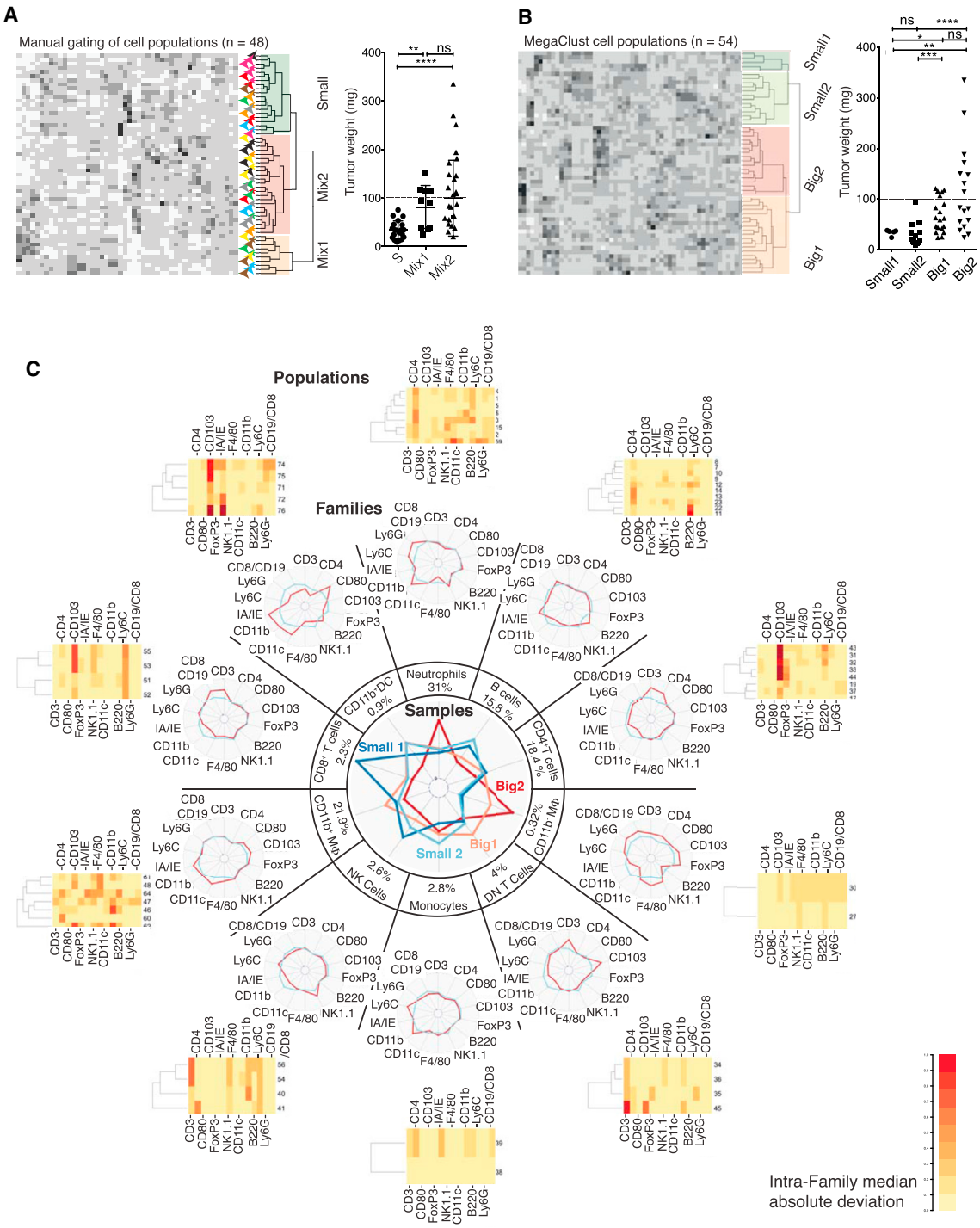

Figure 2. The Immune Signature Identifies a Group of Large Tumors with High Neutrophil and Low B and CD8 T Cell Infiltration

(A and B) Heatmap showing unsupervised hierarchical clustering of individual KP tumors on the basis of their immune signature. (A) Comprising 48 cell populations defined by rational gating; (B) based on MegaClust-derived immune signature comprising 54 cell populations. Dot plot shows the distribution of tumor weight within each group. *p < 0.05, **p < 0.01, ***p < 0.001, and ****p < 0.0001, Mann-Whitney test.

(A) Arrowheads' colors indicate the mouse of origin of the tumors. Three tumor groups were identified: Small (S), Mix1, and Mix2.

(B) Clustering results in two sample groups of small (Small1, Small2) and two groups of large (Big1, Big2) tumors.

(C) Dreamcatcher plot representing MegaClust results. Sample level: central radar plot indicates the relative proportion of each immune cell family identified by MegaClust in Small1, Small2, Big1, and Big2 groups. The average percentage of each family among all annotated immune cells across the 54 samples is

(legend continued on next page)

the proportion of samples' events displaying that population, and (3) its uni-modality on every marker expression. We observed that 43% of MegaClust cell populations were flagged by this quality control, whereas 71% of the populations identified by the gold-standard method viSNE and SPADE were pointed out using the same method (Figures S3A–S3C). Unsupervised hierarchical clustering of the samples on the basis of MegaClust generated four clusters of samples, with two of them containing only small tumors (Small1, n = 5; Small2, n = 13) and two composed of big tumors (Big1, n = 19; Big2, n = 17) (Figure 2B). MegaClust immune signature-derived groups of samples gave a better stratification of tumors regarding their size than manual gating or viSNE and SPADE, which identified a group (V+S 5, n = 19) containing all the biggest lesions (Figure S3D).

To enable a global interpretation, each individual population identified by MegaClust is grouped in families, on the basis of their similarity from hierarchical clustering, and each level of analysis (samples, families, and populations) is represented in a single graph called a dreamcatcher plot. The dreamcatcher plot derived from our 54 KP tumor samples revealed (1) NK and B cell enrichment in Small1 and Small2 compared with Big1 and Big2, (2) a high proportion of $CD8^+$ T cells unique to Small1, and (3) a strong infiltration of neutrophils and $CD11b^-$ macrophages specifically in Big2 (Figure 2C). Manual validation of MegaClust results confirmed these findings (Figure S3E).

On top of predicting tumor size efficiently in tumors originating from the identical oncogenic event, the immune signature highlighted neutrophil enrichment in the biggest tumors. Furthermore, a correlation network between all the immune cell populations indicated that it is the only immune cell type negatively correlated with multiple other populations, suggesting a negative impact of these cells on the anti-tumor immune response (Figure S3F).

$Gr1^+$ Cell Depletion Reduces Lung Tumor Growth, Reverts Immune Exclusion, and Sensitizes Lesions to Anti-PD1 Immunotherapy

To decipher the role of neutrophils in tumors, we aimed at depleting this population using either an anti-Ly6G or anti-Gr1 (Ly6C/G) antibody (ab) in KP mice with well-established tumors. The widely used anti-Ly6G ab (1A8) that binds to neutrophils and masks the Ly6G antigen failed to deplete neutrophils after 1 week of treatment. The anti-Gr1 ab (RB6-8C5) successfully depleted neutrophils in the blood but also decreased circulating monocytes (Figures S4A and S4B). Because we required an efficient neutrophil depletion over several weeks, we decided to pursue our experiments using anti-Gr1 and observed depletion in tumors up to 3 weeks (Figure S4C). Weekly μCT imaging revealed that $Gr1^+$ cell depletion significantly inhibited tumor growth; cancer cell proliferation was diminished and tumor weight was reduced at sacrifice (Figure 3A).

Although neutrophils represent a major population of the tumor immune compartment, $Gr1^+$ cell depletion actually led to an increased tumor infiltration by $CD45^+$ cells (Figure 3B). MegaClust analysis confirmed the successful depletion of neutrophils after 2 weeks of anti-Gr1 treatment, and importantly, the dreamcatcher plot revealed a significant increase in $CD11b^+$ cells, mostly $F4/80^+$ macrophages, indicating that the impact of the anti-Gr1 ab on circulating monocytes does not interfere with macrophage and DC homing in KP tumors. Furthermore, $CD4^+$ T cell infiltration was increased, together with a trend toward $CD8^+$ T cell enrichment (Figure S4D). IF imaging confirmed that $CD8^+$ and $CD4^+$ T cell infiltration into the tumor mass was significantly enhanced (Figure 3C). Additionally, $CD8^+$ T cells proliferated more and Tregs less upon anti-Gr1 treatment (Figure 3D). Our results hence show that depleting $Gr1^+$ cells triggers a profound remodeling of the immune compartment favoring effector T cell enrichment into the tumor mass, suggesting that neutrophils play a role in establishing the immune exclusion of KP tumors.

This prompted us to combine $Gr1^+$ cell depletion with anti-PD1 treatment, as the immune exclusion could explain why immune checkpoint inhibitors are unsuccessful in KP mice (Pfirschke et al., 2016). Although anti-PD1 treatment alone indeed failed to alter tumor progression, anti-PD1 following 1 week of anti-Gr1 led to a stronger reduction of tumor growth compared with $Gr1^+$ depletion alone, with a regression in 42.8% of the lesions (Figure 3E). Consistently, cancer cell death revealed by cleaved caspase-3 (CC3) staining and $CD8^+$ T cell number in the tumor mass were increased by combination therapy and were correlated together (Figure 3F). In addition, the $CD8^+$ T cells' production of interferon-gamma (IFN-γ) was significantly increased compared with anti-Gr1 alone. The effect of anti-PD1 was linked to prior $Gr1^+$ cell depletion, as anti-PD1 treatment alone did not change any of these parameters (Figure S4E). To determine whether the pro-tumor activity of neutrophils resides only in their capability to establish an immune exclusion, we treated KP-Rag^{ko} mice with anti-Gr1. Even in absence of adaptive immunity, $Gr1^+$ cell depletion was still able to reduce tumor growth (Figure 3G). Therefore, we hypothesized that neutrophils contribute to disease progression through an additional mechanism.

$Gr1^+$ Cell Infiltration Associates with Blood Vessel Alteration, Leading to Enhanced Hypoxia and Sustained Snail Expression in Cancer Cells

Considering a recent report demonstrating that blood vessel normalization is a prerequisite for efficient immunotherapy in cancer (Tian et al., 2017), we investigated blood vessel abundance and functionality upon $Gr1^+$ cell depletion. After 2 and 3 weeks of anti-Gr1 treatment, we observed an enrichment of $CD31^+$ endothelial cells and increased vessel coverage by pericytes (αSMA^+) in tumors (Figure 4A). A more detailed analysis of the endothelial cell phenotype revealed a reduction of FasL and an increased intensity of MECA-79 staining, suggesting these vessels are more permissive to immune cell extravasation (Zhang et al., 2005; Motz et al., 2014), which could explain how

indicated. Family level: peripheral radar plots depict the relative expression of each marker by a specific family (red) compared with the average of all the immune cells (blue). The family names were attributed considering their expression of every marker. Population level: heatmaps show individual cell populations within the families on the basis of their deviation from the median expression of each marker across the whole family. White, population is close to the median expression of this marker across the family; red, high degree of deviation from the median marker expression across the family by a population.

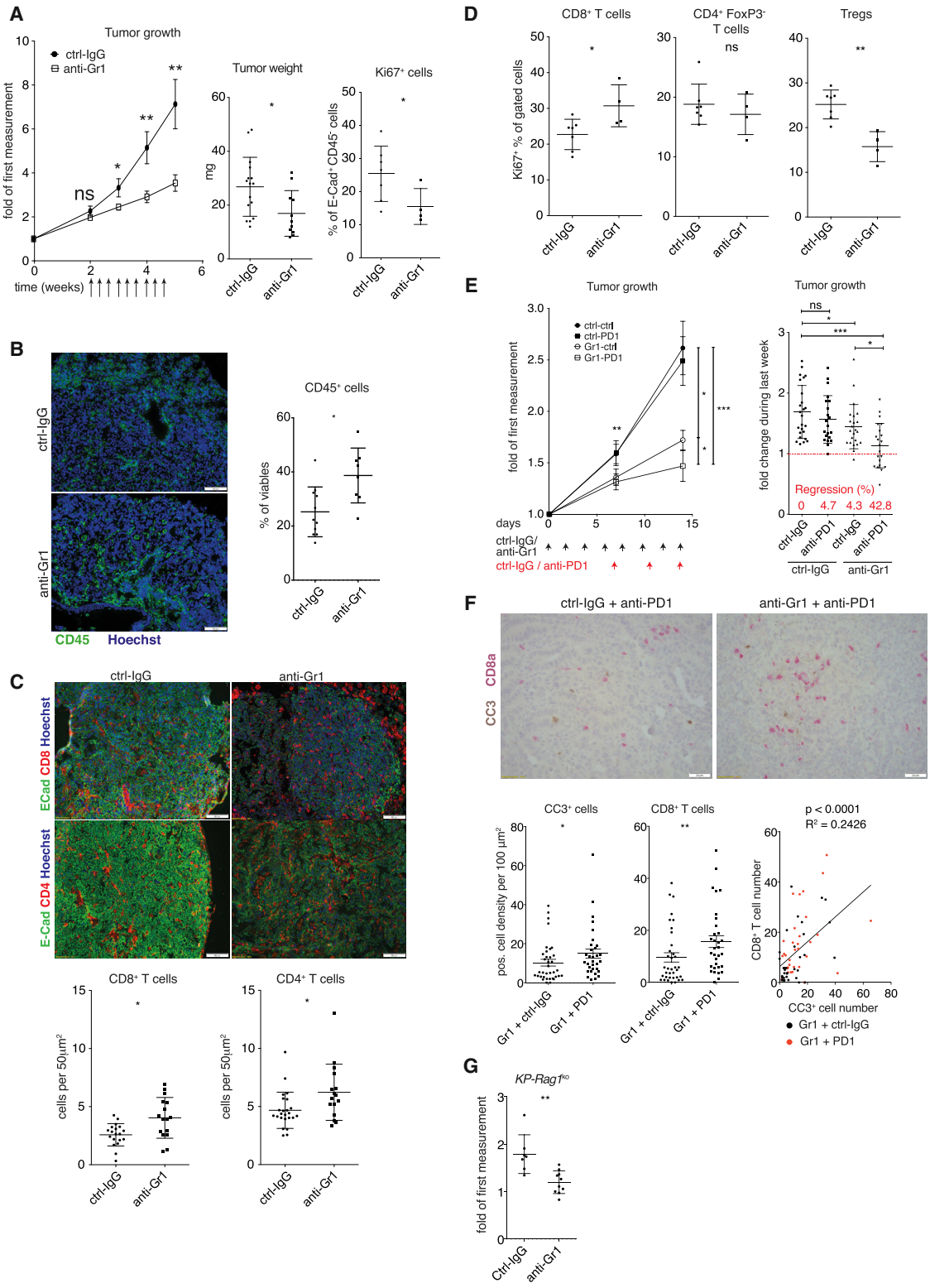

Figure 3. Depletion of Gr1$^+$ Cells Reduces Primary Lung Tumor Growth and Reverts Immune Exclusion

(A) Graph shows growth of control (n = 18) or Gr1$^+$ cell-depleted (n = 19) KP tumors treated for 3 weeks with IgG control or anti-Gr1 from week 2 (administration indicated by arrows). Dot plots represent tumor weight (middle) in the control (n = 16) or anti-Gr1 (n = 11) and the percentage of Ki67$^+$ cells among viable E-cadherin$^+$ CD45$^-$ tumor cells (right) from control (n = 7) tumors or tumors treated with anti-Gr1 (n = 4) for 2 weeks.

(legend continued on next page)

anti-Gr1 treatment reverts the immune exclusion (Figure 4B). Because the tumor vasculature is affected by Gr1$^+$ cell depletion, we speculated that neutrophils contribute to establishing a hypoxic environment. Accordingly, pimonidazole injections revealed diminished hypoxia in Gr1$^+$ cell depleted tumors (Figure 4C).

In order to determine the consequences on tumor cells, we sorted CD45$^-$ cells from KP tumors, composed mostly of E-cadherin-expressing cancer cells, after anti-Gr1 or control ab treatment and performed RNA sequencing. Pathway analysis suggested that Gr1$^+$ cell infiltration enhances cell proliferation (CDC42RAC) and motility (ACTINY) (Figure 4D).

Because Gr1$^+$ cell depletion alleviates hypoxia in KP tumors, we assessed the impact of hypoxia *in vitro* in the human lung cancer cell lines A549 and H2009. Six days of low oxygen pressure (2% O_2) was sufficient to modify the shape of A549 cells from an epithelial- to a mesenchymal-like phenotype (not shown). Time course experiments revealed an increased expression of HIF-1α and the EMT transcription factor Snail from day 2 in both A549 and H2009 cells. ZEB1, another EMT transcription factor and a Snail target, was induced in A549 from day 3. HIF-1α knockdown led to a reduced hypoxia-mediated Snail induction, as shown previously in other cell lines (Yang et al., 2008) (Figures 4E and 4F).

In vivo, we detected decreased Snail protein expression as well as proportion of Snail positive nuclei and lower levels of *Snail* mRNA in CD45$^-$ cells from anti-Gr1-treated tumors (Figures 4G and 4H). These results suggest that neutrophil infiltration, by modifying blood vessels, leads to hypoxia, supporting HIF-1α stabilization, ultimately enhancing Snail expression by tumor cells.

Snail Expression in Cancer Cells Accelerates Disease Progression and Generates Big2-like Tumors

We next wanted to determine whether sustained Snail expression in tumor cells directly contributes to disease progression.

We silenced endogenous Snail in tumor cells using a lentiviral vector coding for Cre and a short hairpin RNA (shRNA) against Snail. Whereas sh1 failed to achieve silencing, sh2 significantly reduced *Snail* mRNA expression compared with normal KP tumors (Cre) (Figure 5A). sh2 uniquely inhibited tumor growth, as no big tumors (>70 mg) developed (Figure 5B).

Then we used a modified version of the KP mice, designated KPR, which express the reverse-tetracycline trans-activator in the lung epithelium (CCSP-rtTA), enabling doxycycline-dependent transgene expression in lung tumor epithelial cells (Meylan et al., 2009). Lung tumors were initiated in KPR and KP (littermate control) mice using lentiviral vectors delivering Cre and doxycycline-inducible Snail. All mice were kept on a doxycycline diet from the day of infection, facilitating Snail expression in the KPR lung tumors (Figure 5C). Disease development was accelerated upon Snail expression: the mice showed reduced survival and a higher proportion of larger and grade 5 tumors and presented with an increased tumor growth rate with enhanced Ki67 expression (Figures 5D–5F). The percentage of Hmga2-positive tumors was increased, while *Ttf1* expression was reduced, indicating loss of tumor differentiation and increased aggressiveness (Winslow et al., 2011) (Figure S5A). *Zeb1* gene expression was increased in Snail-induced tumors. However, although there was a trend toward increased N-cadherin (*Cdh2*) and vimentin (*Vim*), we did not observe changes in any other canonical markers of EMT, including *Twist* and the epithelial marker E-cadherin (*Cdh1*) (Figures S5B and S5C). We observed a modified expression pattern for E-cadherin, with localization rather in the cytoplasm than at the membrane of Snail-positive tumor cells, and histopathological analysis revealed a modest increase in EMT incidence (Figures S5D and S5E). These results altogether point toward the occurrence of a partial EMT phenotype in which an increase of mesenchymal traits coincides with the retention of epithelial characteristics.

Interestingly, comparing the immune cell infiltration of tumors with a similar weight showed that Snail expression by cancer cells led to an elevated percentage of neutrophils (1.7-fold) and reduced B cells (0.62-fold) among immune cells (Figure S6A). By immunohistochemistry with an anti-Ly6G ab, we could confirm an increase in the absolute number of neutrophils in tumors overexpressing Snail (Figure 5G).

For the *in vivo* knockdown experiments, tumors with strong neutrophil infiltration were absent from the *Snail*-sh2 group (Figure 5H), but as a whole there was no significant difference with control and sh1. Hence, sustained Snail expression in tumor cells is at least partly mediated by Gr1$^+$ cell infiltration (see Figures 4G and 4H); in turn, Snail expression in cancer cells generates Big2-like tumors characterized by a large size and low B cell and high neutrophil infiltration.

Snail expression in cancer cells can enhance the recruitment of several immune cell types, such as macrophages (Hsu et al., 2014) or mast cells (Knab et al., 2014), via cytokine production. In an effort to elucidate how Snail expression leads to increased neutrophil infiltration in lung tumors, we assessed the expression

(B) Representative IF images of a control and a Gr1$^+$-depleted tumor showing Hoechst and CD45 staining. The dot plot shows the percentage of CD45$^+$ immune cells among total viable cells from control (n = 11) or anti-Gr1 treated (n = 8) tumors by flow cytometry.
(C) Representative IF staining for CD8 (top) or CD4 (bottom), E-cadherin and Hoechst on control tumors (n = 19), or tumors treated with anti-Gr1 (n = 16) for 2 weeks. Dot plots depict the quantification of positive cells in the tumor mass.
(D) Dot plots indicate the percentage of Ki67$^+$ cells among the respective cell populations (control, n = 7; anti-Gr1, n = 4).
(E) Graph shows the growth of tumors treated with control IgG or anti-Gr1 for 2 weeks with or without combination with anti-PD1 over the second week. Dot plot represents the tumor growth rate during the last week. The percentage of regressing tumors (growth rate < 1×) is indicated. IgG/IgG, n = 21; anti-Gr1/IgG, n = 23; IgG/anti-PD1, n = 22; and anti-Gr1/anti-PD1, n = 22.
(F) Representative double immunohistochemistry (IHC) of CD8 (red) and cleaved caspase-3 (CC3; brown) staining on KP tumor sections from mice treated with anti-Gr1 alone (left) or anti-Gr1 plus anti-PD1 (right). The scale bar represents 20 μm. Dot plots (left and center) represent the density of CC3$^+$ tumor cells or CD8$^+$ T cells within the tumor mass. Correlation plot (right) shows CC3$^+$ and CD8$^+$ T cells association within tumors treated with anti-Gr1 only (black) or the combination (red). The p value and R^2 value are based on Pearson correlation.
(G) Dot plot shows tumor growth in KP-Rag1^{ko} mice treated over 1 week with anti-Gr1 (n = 10) or control IgG (n = 7).
*p < 0.05, **p < 0.01, and ***p < 0.001, Mann-Whitney tests.

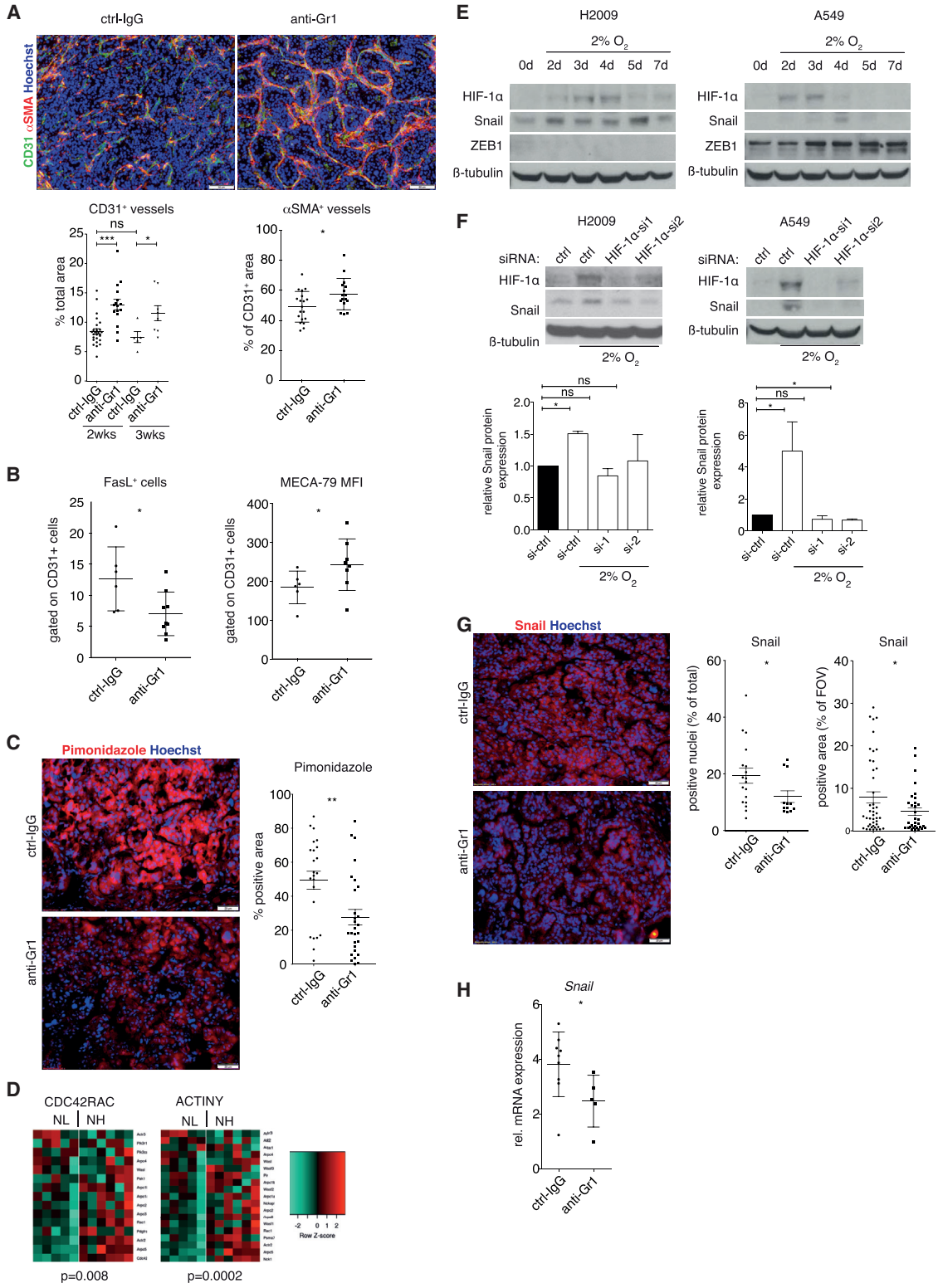

Figure 4. Neutrophil Infiltration Remodels Blood Vessels, Enhancing Hypoxia, and Ultimately Favors Snail Expression in Cancer Cells

(A) Representative IF images of Hoechst, CD31, and αSMA stained tumors. Dot plots indicate (left) the coverage of total area by CD31 staining after 2 or 3 weeks of treatment, in control (n = 26 and n = 5) or anti-Gr1 (n = 15 and n = 8) treated tumors and (right) the αSMA coverage of CD31$^+$ endothelial cells after 2 weeks of treatment (control, n = 17; anti-Gr1, n = 18). The scale bar represents 50 μm.

(legend continued on next page)

of several chemokines (Cxcl1, Cxcl2, and Cxcl5) known to recruit neutrophils. We observed a strong correlation between *Snail* and *Cxcl2* ($p < 0.0001$, $R^2 = 0.832$) in KP tumors (Figure S6B). Furthermore, the secretion of Cxcl2 and Cxcl5 was increased in Snail-expressing tumors (Figure 5I).

To determine the source of these secreted chemokines, we sorted $CD45^-$ and $CD45^+$ cells and observed that the mRNA expression of each of *Cxcl1*, *Cxcl2*, and *Cxcl5* was augmented in both cell compartments of Snail-expressing tumors, with *Cxcl2* expressed mostly by immune cells and *Cxcl5* by tumor cells (Figure S6C). Among tumor-sorted immune cell populations, *Cxcl1* was expressed by monocytes, macrophages, neutrophils, and DCs, whereas *Cxcl2* was produced mostly by neutrophils. *Cxcl1* and *Cxcl2* mRNAs were increased specifically in the sorted neutrophils from Snail tumors (Figure S6D). This suggests a dialog between Snail-expressing tumor cells and neutrophils, resulting in the increased production of neutrophil-recruiting chemokines.

We purified neutrophils from healthy lungs and cultured them in conditioned medium from a murine KP lung cancer cell line (M8), engineered to allow doxycycline-mediated Snail induction. Confirming our hypothesis, the conditioned medium from Snail-expressing cells was able to increase *Cxcl1* and *Cxcl2* mRNA abundance in neutrophils *ex vivo* (Figure 5J). This indicates that Snail-expressing lung cancer cells release a soluble factor, which is detected by neutrophils enhancing neutrophil-homing chemokine production.

Because Snail expression is at least partially dependent on $Gr1^+$ cell recruitment into tumors, we wanted to explore whether the pro-tumor activity of Snail could be due to protection against the adaptive immune response via neutrophil recruitment. We crossed KPR mice to *Rag1*-deficient mice, which revealed that sustained Snail induction increases neutrophil recruitment as in KP tumors and retains pro-tumor activity in mice lacking an adaptive immune system (Figure 5K). Moreover, anti-Gr1 treatment failed to reduce the growth rates of Snail-induced tumors (Figure 5L), demonstrating that Snail favors tumor progression beyond neutrophil recruitment and immune exclusion.

Big2 KP Tumors Reflect a Population of Poor-Prognosis Lung Cancer Patients

We used a tissue microarray (TMA) comprising 150 patient samples with follow-up survival data from the European Thoracic Oncology Platform (ETOP) to analyze B cell ($CD20^+$), neutrophil (polymorphonuclear $CD15^+$), and $CD8^+$ T cell abundance as well as Snail expression. We discovered that a group of patients (group D) mirroring murine group Big2 tumors, characterized by a low proportion of B and $CD8^+$ T cells and a high infiltration with neutrophils, had strongly reduced overall survival ($p = 0.0004$, hazard ratio [HR] = 2.93). In contrast, a group of patients (group A) resembling group Small1, with a high infiltration of $CD8^+$ T cells and B cells and a low infiltration with neutrophils, showed a trend toward improved survival (Figures 6A–6D; Table S3). $CD8^+$ T cell infiltration alone had a tendency toward a good prognosis ($p = 0.1$, HR = 0.61), B cell infiltration was not prognostic, and $CD15^+$ polymorphonuclear neutrophils associated with an adverse outcome ($p = 0.08$, HR = 1.71) (Figures S7A–S7C). In one third of the patients, CD15 was expressed by the tumor cells (Mohammad et al., 2012), and $CD15^+$ tumor cells coincided with a trend toward a better survival ($p = 0.1$, HR = 0.62) (Figures S7D and S7E). In accordance with Big2 mouse tumors, patients from group D presented with bigger tumors at the time of biopsy (Figure 6E). Furthermore, neutrophil infiltration and CD31 staining were negatively correlated (Figure 6F). We also confirmed that Snail expression is associated with an adverse outcome ($p = 0.05$, HR = 1.83) (Figure 6G), as reported previously (Hung et al., 2009; Yanagawa et al., 2009). Groups of patients showing higher infiltration of neutrophils also displayed increased proportion of Snail-positive tumors (Figure S7F). In The Cancer Genome Atlas, *SNAIL* was positively correlated with the expression of each of *CXCL1*, *CXCL2*, *CXCL5*, and *CXCL8* mRNA in lung adenocarcinoma patients (Figure S7G). In conclusion, translation of our findings from the KP mouse model to human lung adenocarcinoma uncovers a group comprising about one third of lung adenocarcinoma patients displaying larger tumors with a high neutrophil infiltration and a poor prognosis.

DISCUSSION

Similarly to NSCLC patients (Dieu-Nosjean et al., 2014), well-organized TLS-like structures are formed in the lung of tumor-bearing mice (Joshi et al., 2015). To interrogate the contribution of the immune compartment in this disease, we have developed a powerful algorithm, MegaClust, allowing us to generate an immune signature of lung tumors. Neutrophils are most abundant in

(B) Flow cytometry analysis of FasL and MECA-79 within gated $CD31^+$ endothelial cells from control (n = 6) or anti-Gr1-treated (n = 9) tumors.
(C) Representative fluorescence images of pimonidazole and Hoechst staining of control (n = 31) tumors or tumors treated with anti-Gr1 for 2 weeks (n = 32). Dot plot indicates the percentage of hypoxic area in pimonidazole-positive tumors (>1% $pimonidazole^+$ area) in both groups in similar size tumors. The scale bar represents 20 μm.
(D) Heatmaps representing the results from RNA sequencing of non-immune $CD45^-$ tumor cell fractions from $neutrophil^{low}$ (NL) and $neutrophil^{high}$ (NH) KP tumors, showing reduced CDC42 and ACTINY pathways (Biocarta) in NL tumors.
(E) H2009 and A549 cells were cultured under normoxia or hypoxia for up to 6 days. Western blot (WB) shows expression of HIF1-α, Snail, ZEB1, and β-tubulin (loading control) at the indicated time point.
(F) H2009 and A549 cells were transfected with control small interfering RNA (siRNA) or siRNA against HIF-1α, followed by culture under normoxia or hypoxia for 48 hr. WB shows the expression of HIF-1α, Snail, and β-tubulin. Histograms show Snail protein quantification from four independent experiments (mean ± SEM).
(G) Representative IF images of Snail and Hoechst staining on control tumors (n = 46) and tumors treated with anti-Gr1 (n = 32) for 2 weeks. The left dot plot indicates the extent of Snail staining within the nuclei in tumors with detectable Snail (>5% of $Snail^+$ area). The right dot plot shows the percentage of Snail-positive area within a field of view (FOV).
(H) Dot plot shows the levels of *Snail* gene expression in $CD45^-$ sorted cell fractions from KP tumors after 2 weeks of control IgG (n = 9) or anti-Gr1 (n = 5) treatment.
In (A)–(C) and (F)–(H), *$p < 0.05$, **$p < 0.01$, and ***$p < 0.001$, Mann-Whitney tests.

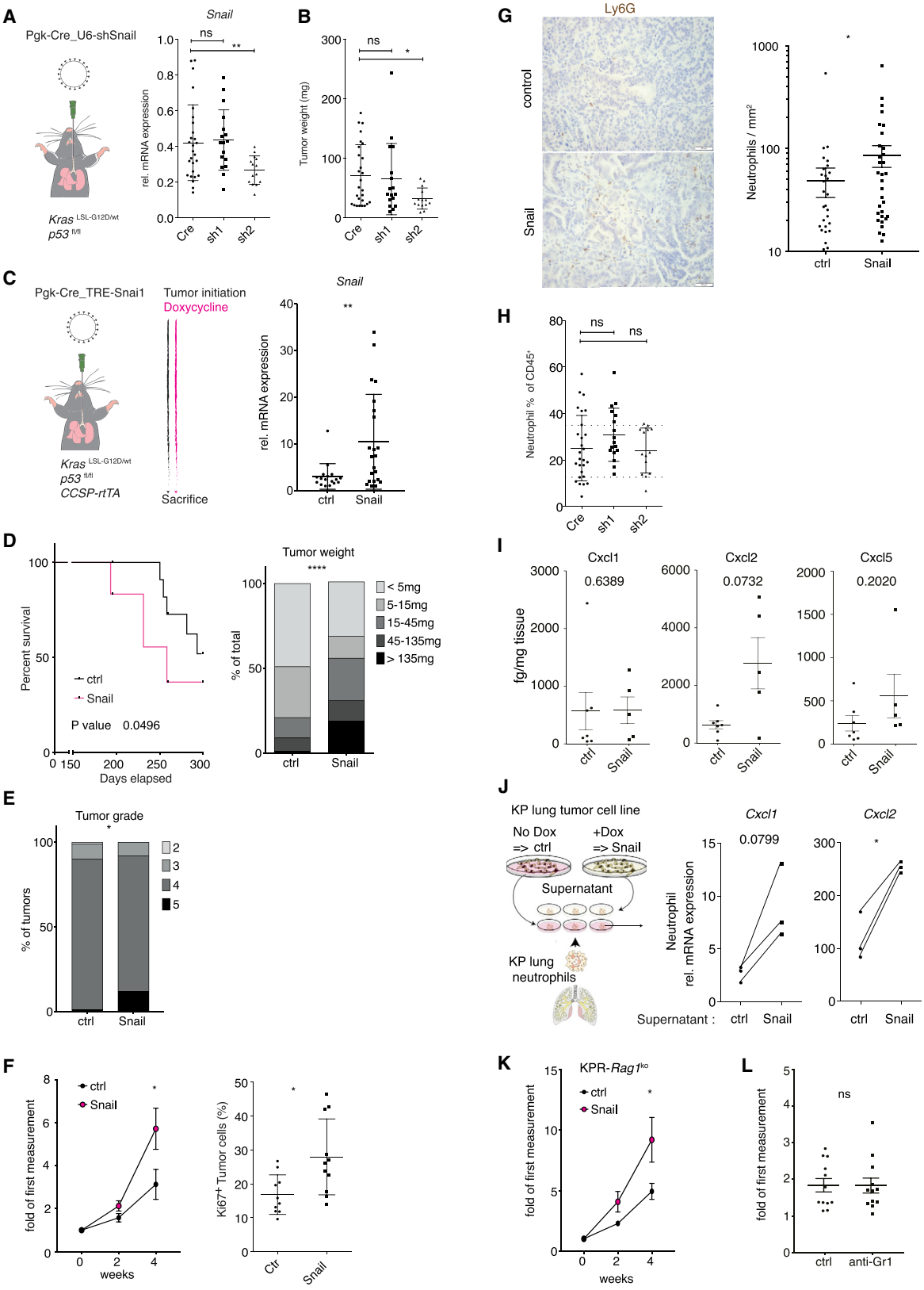

(legend on next page)

a subgroup of large and hence advanced tumors. By integrating patient samples, we could confirm that neutrophils have a strong association with disease progression, consistent with a previous report (Peng et al., 2015). Although neutrophils participate in breast cancer metastasis to the lung (Coffelt et al., 2015; Wculek and Malanchi, 2015), their role in the biology of primary lung tumors remains obscure.

Our work revealed technical difficulties inherent to the functional characterization of neutrophils *in vivo*. We compared the efficacy of two commonly used antibodies, anti-Ly6G and anti-Gr1, to specifically deplete these cells and observed that neither of them yielded satisfactory results. Only anti-Gr1 resulted in a good depletion of neutrophils but was accompanied by off-target effects on monocytes. However, the monocyte infiltration in KP tumors is intrinsically very low, and $CD11b^+$ cell infiltration in tumors was not reduced by anti-Gr1. Nevertheless, there is a need to develop better tools to further understand the functionality of these cells in cancer.

Our results demonstrate that neutrophil infiltration orchestrates the immune exclusion in KP tumors, leading to failure of immunotherapy. Considering that KP tumors present a very small number of secondary mutations, one could hypothesize that immunotherapy success is prevented by the lack of tumor antigens to target (Westcott et al., 2015). We show here that tumors grow faster in a $Rag1^{ko}$ background, suggesting a partial control of the lesions by adaptive immunity. Furthermore, it has been reported that even the immunogenic variant of this model, generated by introducing strong antigens (luciferase or ovalbumin), remains insensitive to anti-PD1 (Pfirschke et al., 2016). Whereas old paradigms stipulated that tumors can be either detected or ignored by the immune system, more recent observations have proposed the existence of a third group of lesions in which the immune cells are excluded from the tumor mass, rendering them resistant to immune checkpoint blockade (Joyce and Fearon, 2015; Topalian et al., 2016). Consistently, we observed that $Gr1^+$ cell depletion modified blood vessels by enhancing their spreading and coverage by pericytes, in line with a previous study in a pancreatic cancer model (Incio et al., 2016). Furthermore, in absence of neutrophils, endothelial cells acquire a HEV-like phenotype that could participate in immune cell extravasation into the tumor mass (Sata and Walsh, 1998). This could explain the reversal of the immune exclusion due to a mutual regulation between blood vessel normalization and immune reprograming (Tian et al., 2017).

Our results, however, suggest that the immune exclusion only partially explains the tumor-promoting effect of neutrophils, as even in the absence of adaptive immunity, neutrophils promote tumor growth. Through its action on blood vessels, neutrophil infiltration increases tumor hypoxia. Our *in vitro* experiments demonstrated that hypoxia, via HIF-1α, stabilizes Snail expression in tumor cells. Accordingly, $Gr1^+$ cell depletion led to a reduction of both hypoxia and Snail expression in KP tumors. This observation goes in line with a previous report showing that expression of a non-degradable mutant form of HIF-2α in Kras-driven lung tumors stabilizes Snail expression (Kim et al., 2009). We functionally demonstrated that enhanced Snail accelerates lung cancer progression, which is consistent with its negative prognostic value in lung cancer (Hung et al., 2009; Yanagawa et al., 2009). This indicates that in addition to the immune exclusion and blood vessel remodeling, neutrophils favor disease progression by stabilizing Snail.

Previous reports have established a role for Snail in supporting tumor development and progression via cytokine production and the recruitment of specific immune cell populations, ultimately promoting a pro-tumorigenic immune microenvironment in various contexts (Hsu et al., 2014; Kudo-Saito et al., 2009). Our results indicate that Snail activity in lung tumor cells enhances neutrophil recruitment into the tumor mass. Snail-expressing tumor cells release a soluble factor that enhances the secretion of Cxcl2 in the tumor microenvironment, thereby establishing a positive feedback loop of Snail-mediated neutrophil recruitment. Although this probably involves multiple mechanisms, Cxcr2, the

Figure 5. Snail Expression in Cancer Cells Accelerates Disease Progression and Increases Tumor Neutrophil Infiltration

(A) Schematic view of Snail silencing in the KP model using a lentiviral vector facilitating constitutive shRNA expression. The dot plot shows *Snail* mRNA expression in control (Cre) tumors or tumors expressing one of two shRNAs to target Snail with only one, sh2, which is effective 23 weeks after tumor initiation.

(B) Dot plot represents tumor weight at sacrifice of control, sh1, or sh2. In (A) and (B), Cre, n = 27; sh1, n = 17; and sh2, n = 14.

(C) Schematic view of the KPR model allowing doxycycline-mediated Snail induction in the lung tumor cells (Tet-ON). Doxycycline was administered via the diet from the day of tumor initiation. Dot plot shows *Snail* mRNA expression in whole-tumor extracts of KP (control, n = 17) and KPR (Snail-induced, n = 22) mice 16 weeks after tumor initiation.

(D) Left: survival curves of control (n = 15) or Snail-overexpressing (n = 12) mice on the basis of the development of a lung tumor burden compelling sacrifice of the mice or actual death. Right: histogram showing the repartition of the tumors in five groups according to their weight at sacrifice. ****$p < 0.0001$, chi-square test.

(E) Histograms representing the quantification of the tumor grade (1–5) in control or Snail-induced tumors. *$p < 0.05$, chi-square test.

(F) Left: evolution of tumor volume over 4 weeks in control (n = 7) or Snail-overexpressing (n = 10) tumors. Right: dot plot shows percentage of $Ki67^+$ cells among viable $CD45^-$ E-cadherin$^+$ KP cancer cells from tumors overexpressing Snail (KPR, n = 11) or control (KP, n = 10).

(G) Representative IHC of control (n = 34) or Snail-overexpressing (n = 35) tumors showing neutrophil infiltration on the basis of Ly6G staining. The scale bar represents 20 μm. Dot plot represents the neutrophil density in the tumors.

(H) Dot plot represents the percentage of neutrophils among $CD45^+$ cells of control, sh1, or sh2 tumors. Dashed lines show the first and third quartiles.

(I) ELISA-based quantification of Cxcl1, Cxcl2, and Cxcl5 chemokine secretion in control (n = 7) and Snail-overexpressing (n = 5) tumors performed on tissue dissociation supernatant.

(J) *Cxcl1* and *Cxcl2* mRNA expression in neutrophils extracted from healthy lungs and incubated for 14 hr with conditioned medium from a KP lung cancer cell line (M8) engineered to enable doxycycline-mediated Snail induction.

(K) The graph depicts the evolution of tumor volumes over 2 and 4 weeks, relative to the first measurement performed at 22 weeks post-tumor initiation, in control (no doxycycline, n = 14) or Snail-overexpressing (doxycycline, n = 16) tumors from *Rag1*-deficient KPR mice.

(L) Dot plot shows the growth of Snail-overexpressing tumors treated (n = 12) or untreated (n = 12) with anti-Gr1 for 2 weeks.

In (A)–(C) and (F)–(K), *$p < 0.05$ and **$p < 0.01$, Mann-Whitney test.

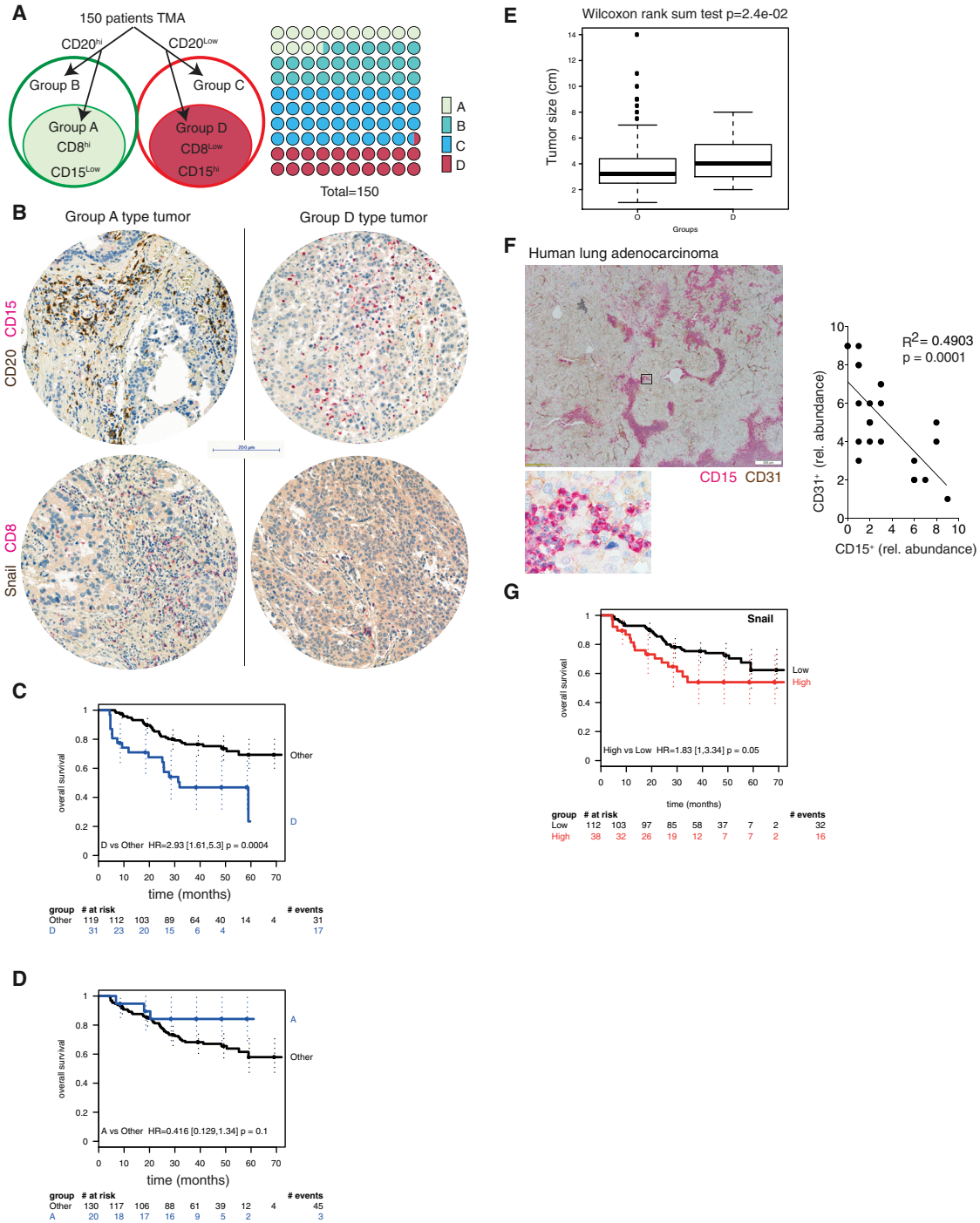

Figure 6. Big2 KP Tumors Recapitulate a Subset of Lung Adenocarcinomas Associated with Poor Patient Prognosis

(A) Schematic classification of the patients (n = 150) into groups A–D on the basis of TMA analyses of $CD8^+$, $CD20^+$, and polymorphonuclear $CD15^+$ cells in tumors. Group A reflects mouse Small1; group B, high B cells minus group A; group C, low B cells minus group D; and group D, mouse Big2.

(B) IHC of TMA samples representative of group A and group D patients. Top: CD15 and CD20 co-staining; bottom: CD8 and Snail co-staining. The scale bar represents 200 μm.

(C and D) Survival curves of group A (C) or group D (D) patients versus all others.

(E) Boxplot showing tumor size at the day of biopsy in group D patients versus all others (O).

(F) Representative double IHC for CD15 and CD31 on a human lung tumor section. The scale bar represents 200 μm. The scatterplot and linear regression display the correlation between neutrophils (CD15) and blood vessels (CD31) (n = 18). The p value and R^2 value are based on Pearson correlation.

(G) Overall survival of patients according to Snail expression in the tumors (cutoff ≥ 3).

receptor for Cxcl1, Cxcl2, and Cxcl5, has been shown to participate in neutrophil recruitment in pancreatic tumors (Steele et al., 2016). As exemplified by Cxcl2 expression by tumor neutrophils, Snail-expressing cancer cells could release chemokines and cytokines that modify neutrophil behavior. Identifying the soluble factor(s) leading to exacerbated Cxcl2 expression by neutrophils in tumors is a potential important perspective that could open for new therapeutic approaches.

Given that we have also observed a tumor growth-promoting effect of Snail in immunodeficient *Rag1*^{ko} mice and that neutrophil depletion did not affect tumor growth kinetics of Snail-overexpressing tumors, Snail probably exerts additional tumor-promoting functions beyond its role in modulating the tumor immune compartment. The detrimental role of Snail in cancer classically includes the facilitation of metastatic progression of tumors via EMT (Thiery et al., 2009). We did indeed detect a reduced membrane E-cadherin localization in regions of strong Snail expression and a concomitant increase in some mesenchymal markers, consistent with a partial EMT phenotype (Nieto et al., 2016).

In conclusion, we demonstrate the clinical relevance of drawing an unsupervised immune signature from murine tumor samples, as this enabled us to characterize a mechanism of immune exclusion and disease progression driven by neutrophils. We are hence proposing a deleterious dialogue among neutrophils, blood vessels, and cancer cells, culminating in the stabilization of Snail in tumor cells and the establishment of a tumor microenvironment favoring disease progression.

EXPERIMENTAL PROCEDURES

All reagents (Ab, oligonucleotides), lentiviral vector construction and production, flow cytometry staining, MegaClust processing, and details on immunostaining are given in Supplemental Experimental Procedures.

Mouse Models

K-ras$^{LSL\text{-}G12D/WT}$ and *p53*$^{FL/FL}$ mice in a C57BL6/J background were bred to obtain *K-ras*$^{LSL\text{-}G12D/WT}$; *p53*$^{FL/FL}$ (KP) mice. KP mice were bred with *CCSP-rtTA* (R) mice in the same background to generate KPR mice. KPR mice were bred with *Rag1*$^{-/-}$ animals to generate immunodeficient KPR mice. K, P, and R mice were purchased from The Jackson Laboratory. All mouse experiments were performed with the permission of the Veterinary Authority of Canton de Vaud, Switzerland (license number VD2391). All experimental design, animal housing conditions, animal number, and treatment modalities were previously approved by Réseau des Animaleries Lémaniques (RESAL) competent ethics committee.

Mouse Treatment Modalities

The tumors were initiated upon infection of lung epithelial cells with a viral vector delivering Cre recombinase to activate oncogenic *Kras*^{G12D} and delete *p53* (Jackson et al., 2005). Twelve- to fourteen-week-old mice were infected intratracheally with 1,500 Cre-active lentiviral units. Neutrophil depletion was performed at 25 weeks post-tumor initiation (WPI) using anti-Ly6G or anti-Gr1 ab (10 mg/kg) three times per week. Neutrophil depletion was validated during the experiment by tail vain blood sampling at day 12, followed by flow cytometry analyses of $CD11b^+Ly6C^+CD11c^-Ly6G^+$ circulating cells. Control mice were injected with IgG ab at the same dose (Jackson Immunoresearch). For the pimonidazole treatment, mice received 50 μL/10 g of 12 mg/mL pimonidazole solution intraperitoneally (i.p.) 1 hr before sacrifice. For Snail induction, the mice were fed a diet containing 0.625 g/kg doxycycline (Provimi Kliba) from the day of tumor initiation until the day of sacrifice.

To measure tumor volume, mice were anaesthetized using isoflurane and maintained under anesthesia during the scanning procedure. Lungs were imaged with μCT (Quantum FX; PerkinElmer) at a 50 μm voxel size, with retrospective respiratory gating. Individual tumor volumes were measured and calculated using Analyze (PerkinElmer).

Chemokine Measurements

Tumors were mechanically dissociated in 200 μL DMEM per 50 mg tissue. Supernatant was generated by centrifugation, filtered, and stored at −80°C. Chemokine quantification was done using the LEGENDPlex proinflammatory chemokine multiplex assay (740451; Biolegend) according to the provider's instructions and analyzed using the dedicated software provided by Biolegend. Data acquisition was performed on a LSRII SORP flow cytometer with HTS module. For Cxcl2, we used the mouse Quantikine ELISA kit (MM200).

TCGA Data Processing

The Cancer Genome Atlas (TCGA) Lung Adenocarcinoma (LUAD) dataset was retrieved from http://cancergenome.nih.gov. Samples with clinical information and mRNA (RNASEQV2) expression data were selected (448 samples), and the data were downloaded using the RTCGA package (Samur, 2014). Normalized RSEM gene counts as provided by TCGA were taken. As a filtering step, only genes with counts per million >1 in at least 50 samples were kept for further analysis, and counts were converted to log-counts per million using the voom function from the limma package (Ritchie et al., 2015).

Mouse mRNA Sequencing, Differential Expression, and Pathway Analyses

Multiplexed libraries for mRNA sequencing (mRNA-seq) were prepared with the TruSeq stranded mRNA kit (Illumina) starting from 500 ng of good-quality total RNAs (RNA quality scores >7 on the Fragment Analyzer). Sequencing was subsequently performed on a NextSeq 500 instrument (Illumina) on a high-output flow cell, yielding single-end reads of 85 nucleotides. Adaptor sequences and low-quality ends were removed with cutadapt version 1.4.2, trimming for TrueSeq and polyA sequences. Reads were aligned to mouse genome build mm10 using STAR aligner.

Differential expression between neutrophil^{high} (NH) and neutrophil^{low} (NL) samples (determined by flow cytometry) was computed with DEseq2, after filtering genes with average counts < 5. Gene set enrichment analysis was performed on the ranked list of genes with Biocarta genesets.

Statistics

For all mouse experiments, we used a minimum of four mice per condition, and n refers to the number of tumors analyzed. All results are represented as mean ± SEM if not stated otherwise. Comparisons between groups were made as stated in the figure legends. Statistical significance is indicated as *$p < 0.05$, **$p < 0.01$, ***$p < 0.001$, ****$p < 0.0001$, or ns (not significant), using Mann-Whitney tests because of small group size, where not indicated otherwise. Statistical analysis was performed using Prism 6 software.

For human data, all statistical analyses were performed using the free high-level interpreted statistical language R (version 3.2.2) and various Bioconductor packages (http://www.bioconductor.org).

Data and Software Availability

For MegaClust usage, please see http://megaclust.vital-it.ch. The accession number for the RNA sequencing data reported in this paper is GEO: GSE87681.

SUPPLEMENTAL INFORMATION

Supplemental Information includes Supplemental Experimental Procedures, seven figures, and three tables and can be found with this article online at https://doi.org/10.1016/j.celrep.2017.11.052.

ACKNOWLEDGMENTS

We thank Dr. R. Colisson and Profs. F. Radtke and M. Pittet for critical reading of the manuscript and T. Imler for technical help. We thank the Ecole Polytechnique Fédérale de Lausanne (EPFL) SV Histology, Bioimaging and Optics, and

Flow Cytometry Core Facilities for access to instruments and help in analyses; the Gene Expression Core Facility for RNA sequencing; and the University of Bern Translational Research Unit of the Institute of Pathology, especially Dr. J. Galvan, for help with the human tissue sections. We thank the ETOP Lungscape team for generously providing the TMA and Dr. L. B. Madsen (Aarhus University) for cutting the slides. This work was supported by the Swiss National Science Foundation, National Centre of Competence in Research (NCCR) Molecular Oncology, the Swiss Cancer League (KLS-2885-02-2012), the Chercher et Trouver Foundation, a "Molecular Life Sciences" grant from the ISREC Foundation (to S.G.), and the Nuovo Soldati Foundation (to G.B.).

AUTHOR CONTRIBUTIONS

J.F., S.G., and E.M. conceived the study. J.F. performed experiments on neutrophils with assistance from G.B. (necropsy and IF) and M.G. (flow cytometry). S.G. developed Snail-inducible mouse model and characterized Snail biology *in vivo* with J.F. and L.S. M.S., N.G., and I.X. performed the development of and analysis with MegaClust. N.Z. performed the bioinformatics analyses from TCGA. A.P. performed histopathological analyses for mouse samples and I.Z. for human samples. All authors contributed to data analyses and discussion. J.F. and S.G. wrote the manuscript, and E.M. edited it. E.M. supervised the study.

DECLARATION OF INTERESTS

The authors declare no competing interests.

Received: April 25, 2017
Revised: October 19, 2017
Accepted: November 15, 2017
Published: December 12, 2017

REFERENCES

Coffelt, S.B., Kersten, K., Doornebal, C.W., Weiden, J., Vrijland, K., Hau, C.-S., Verstegen, N.J.M., Ciampricotti, M., Hawinkels, L.J.A.C., Jonkers, J., and de Visser, K.E. (2015). IL-17-producing γδ T cells and neutrophils conspire to promote breast cancer metastasis. Nature *522*, 345–348.

Dieu-Nosjean, M.-C., Goc, J., Giraldo, N.A., Sautès-Fridman, C., and Fridman, W.H. (2014). Tertiary lymphoid structures in cancer and beyond. Trends Immunol. *35*, 571–580.

DuPage, M., Cheung, A.F., Mazumdar, C., Winslow, M.M., Bronson, R., Schmidt, L.M., Crowley, D., Chen, J., and Jacks, T. (2011). Endogenous T cell responses to antigens expressed in lung adenocarcinomas delay malignant tumor progression. Cancer Cell *19*, 72–85.

Ferlay, J., Soerjomataram, I., Dikshit, R., Eser, S., Mathers, C., Rebelo, M., Parkin, D.M., Forman, D., and Bray, F. (2015). Cancer incidence and mortality worldwide: sources, methods and major patterns in GLOBOCAN 2012. Int. J. Cancer *136*, E359–E386.

Galon, J., Costes, A., Sanchez-Cabo, F., Kirilovsky, A., Mlecnik, B., Lagorce-Pagès, C., Tosolini, M., Camus, M., Berger, A., Wind, P., et al. (2006). Type, density, and location of immune cells within human colorectal tumors predict clinical outcome. Science *313*, 1960–1964.

Goc, J., Fridman, W.-H., Sautès-Fridman, C., and Dieu-Nosjean, M.-C. (2013). Characteristics of tertiary lymphoid structures in primary cancers. OncoImmunology *2*, e26836.

Hsu, D.S.-S., Wang, H.-J., Tai, S.-K., Chou, C.-H., Hsieh, C.-H., Chiu, P.-H., Chen, N.-J., and Yang, M.-H. (2014). Acetylation of snail modulates the cytokinome of cancer cells to enhance the recruitment of macrophages. Cancer Cell *26*, 534–548.

Hung, J.-J., Yang, M.-H., Hsu, H.-S., Hsu, W.-H., Liu, J.-S., and Wu, K.-J. (2009). Prognostic significance of hypoxia-inducible factor-1α, TWIST1 and Snail expression in resectable non-small cell lung cancer. Thorax *64*, 1082–1089.

Incio, J., Liu, H., Suboj, P., Chin, S.M., Chen, I.X., Pinter, M., Ng, M.R., Nia, H.T., Grahovac, J., Kao, S., et al. (2016). Obesity-induced inflammation and desmoplasia promote pancreatic cancer progression and resistance to chemotherapy. Cancer Discov. *6*, 852–869.

Jackson, E.L., Olive, K.P., Tuveson, D.A., Bronson, R., Crowley, D., Brown, M., and Jacks, T. (2005). The differential effects of mutant p53 alleles on advanced murine lung cancer. Cancer Res. *65*, 10280–10288.

Joshi, N.S., Akama-Garren, E.H., Lu, Y., Lee, D.-Y., Chang, G.P., Li, A., DuPage, M., Tammela, T., Kerper, N.R., Farago, A.F., et al. (2015). Regulatory T cells in tumor-associated tertiary lymphoid structures suppress anti-tumor T cell responses. Immunity *43*, 579–590.

Joyce, J.A., and Fearon, D.T. (2015). T cell exclusion, immune privilege, and the tumor microenvironment. Science *348*, 74–80.

Kim, W.Y., Perera, S., Zhou, B., Carretero, J., Yeh, J.J., Heathcote, S.A., Jackson, A.L., Nikolinakos, P., Ospina, B., Naumov, G., et al. (2009). HIF2α cooperates with RAS to promote lung tumorigenesis in mice. J. Clin. Invest. *119*, 2160–2170.

Knab, L.M., Ebine, K., Chow, C.R., Raza, S.S., Sahai, V., Patel, A.P., Kumar, K., Bentrem, D.J., Grippo, P.J., and Munshi, H.G. (2014). Snail cooperates with Kras G12D in vivo to increase stem cell factor and enhance mast cell infiltration. Mol. Cancer Res. *12*, 1440–1448.

Kudo-Saito, C., Shirako, H., Takeuchi, T., and Kawakami, Y. (2009). Cancer metastasis is accelerated through immunosuppression during Snail-induced EMT of cancer cells. Cancer Cell *15*, 195–206.

Martinet, L., Le Guellec, S., Filleron, T., Lamant, L., Meyer, N., Rochaix, P., Garrido, I., and Girard, J.-P. (2012). High endothelial venules (HEVs) in human melanoma lesions. Oncoimmunology *1*, 829–839.

Meylan, E., Dooley, A.L., Feldser, D.M., Shen, L., Turk, E., Ouyang, C., and Jacks, T. (2009). Requirement for NF-kappaB signalling in a mouse model of lung adenocarcinoma. Nature *462*, 104–107.

Mohammad, T., Garratt, J., Torlakovic, E., Gilks, B., and Churg, A. (2012). Utility of a CEA, CD15, calretinin, and CK5/6 panel for distinguishing between mesotheliomas and pulmonary adenocarcinomas in clinical practice. Am. J. Surg. Pathol. *36*, 1503–1508.

Motz, G.T., Santoro, S.P., Wang, L.-P., Garrabrant, T., Lastra, R.R., Hagemann, I.S., Lal, P., Feldman, M.D., Benencia, F., and Coukos, G. (2014). Tumor endothelium FasL establishes a selective immune barrier promoting tolerance in tumors. Nat. Med. *20*, 607–615.

Nieto, M.A., Huang, R.Y.-J., Jackson, R.A., and Thiery, J.P. (2016). EMT: 2016. Cell *166*, 21–45.

Peng, B., Wang, Y.-H., Liu, Y.-M., and Ma, L.-X. (2015). Prognostic significance of the neutrophil to lymphocyte ratio in patients with non-small cell lung cancer: a systemic review and meta-analysis. Int. J. Clin. Exp. Med. *8*, 3098–3106.

Pfirschke, C., Engblom, C., Rickelt, S., Cortez-Retamozo, V., Garris, C., Pucci, F., Yamazaki, T., Poirier-Colame, V., Newton, A., Redouane, Y., et al. (2016). Immunogenic chemotherapy sensitizes tumors to checkpoint blockade therapy. Immunity *44*, 343–354.

Reck, M., Rodríguez-Abreu, D., Robinson, A.G., Hui, R., Csőszi, T., Fülöp, A., Gottfried, M., Peled, N., Tafreshi, A., Cuffe, S., et al.; KEYNOTE-024 Investigators (2016). Pembrolizumab versus chemotherapy for PD-L1-positive non-small-cell lung cancer. N. Engl. J. Med. *375*, 1823–1833.

Ritchie, M.E., Phipson, B., Wu, D., Hu, Y., Law, C.W., Shi, W., and Smyth, G.K. (2015). limma powers differential expression analyses for RNA-sequencing and microarray studies. Nucleic Acids Res. *43*, e47.

Samur, M.K. (2014). RTCGAToolbox: a new tool for exporting TCGA Firehose data. PLoS ONE *9*, e106397.

Sata, M., and Walsh, K. (1998). TNFalpha regulation of Fas ligand expression on the vascular endothelium modulates leukocyte extravasation. Nat. Med. *4*, 415–420.

Steele, C.W., Karim, S.A., Leach, J.D.G., Bailey, P., Upstill-Goddard, R., Rishi, L., Foth, M., Bryson, S., McDaid, K., Wilson, Z., et al. (2016). CXCR2 inhibition

profoundly suppresses metastases and augments immunotherapy in pancreatic ductal adenocarcinoma. Cancer Cell *29*, 832–845.

Thiery, J.P., Acloque, H., Huang, R.Y.J., and Nieto, M.A. (2009). Epithelial-mesenchymal transitions in development and disease. Cell *139*, 871–890.

Tian, L., Goldstein, A., Wang, H., Ching Lo, H., Sun Kim, I., Welte, T., Sheng, K., Dobrolecki, L.E., Zhang, X., Putluri, N., et al. (2017). Mutual regulation of tumour vessel normalization and immunostimulatory reprogramming. Nature *544*, 250–254.

Topalian, S.L., Taube, J.M., Anders, R.A., and Pardoll, D.M. (2016). Mechanism-driven biomarkers to guide immune checkpoint blockade in cancer therapy. Nat. Rev. Cancer *16*, 275–287.

Wculek, S.K., and Malanchi, I. (2015). Neutrophils support lung colonization of metastasis-initiating breast cancer cells. Nature *528*, 413–417.

Westcott, P.M.K., Halliwill, K.D., To, M.D., Rashid, M., Rust, A.G., Keane, T.M., Delrosario, R., Jen, K.-Y., Gurley, K.E., Kemp, C.J., et al. (2015). The mutational landscapes of genetic and chemical models of Kras-driven lung cancer. Nature *517*, 489–492.

Winslow, M.M., Dayton, T.L., Verhaak, R.G.W., Kim-Kiselak, C., Snyder, E.L., Feldser, D.M., Hubbard, D.D., DuPage, M.J., Whittaker, C.A., Hoersch, S., et al. (2011). Suppression of lung adenocarcinoma progression by Nkx2-1. Nature *473*, 101–104.

Yanagawa, J., Walser, T.C., Zhu, L.X., Hong, L., Fishbein, M.C., Mah, V., Chia, D., Goodglick, L., Elashoff, D.A., Luo, J., et al. (2009). Snail promotes CXCR2 ligand-dependent tumor progression in non-small cell lung carcinoma. Clin. Cancer Res. *15*, 6820–6829.

Yang, M.-H., Wu, M.-Z., Chiou, S.-H., Chen, P.-M., Chang, S.-Y., Liu, C.-J., Teng, S.-C., and Wu, K.-J. (2008). Direct regulation of TWIST by HIF-1α promotes metastasis. Nat. Cell Biol. *10*, 295–305.

Zhang, W., Ding, E.-X., Wang, Q., Zhu, D.-Q., He, J., Li, Y.-L., and Wang, Y.-H. (2005). Fas ligand expression in colon cancer: a possible mechanism of tumor immune privilege. World J. Gastroenterol. *11*, 3632–3635.